Stellar Characterization of M Dwarfs from the APOGEE Survey: A Calibrator Sample for M-dwarf Metallicities

Diogo Souto[1,2] , Katia Cunha[2,3] , Verne V. Smith[4], C. Allende Prieto[5,6] , Adam Burgasser[7] , Kevin Covey[8] ,
D. A. García-Hernández[5,6] , Jon A. Holtzman[9] , Jennifer A. Johnson[10] , Henrik Jönsson[11,12] , Suvrath Mahadevan[13] ,
Steven R. Majewski[14] , Thomas Masseron[5,6], Matthew Shetrone[15] , Bárbara Rojas-Ayala[16], Jennifer Sobeck[14],
Keivan G. Stassun[17] , Ryan Terrien[18] , Johanna Teske[19,20], Fábio Wanderley[2], and Olga Zamora[5,6]

[1] Departamento de Física, Universidade Federal de Sergipe, Av. Marechal Rondon, S/N, 49000-000 São Cristóvão, SE, Brazil
souto@on.br, diogodusouto@gmail.com
[2] Observatório Nacional/MCTIC, R. Gen. José Cristino, 77, 20921-400, Rio de Janeiro, Brazil
[3] Steward Observatory, University of Arizona, 933 North Cherry Avenue, Tucson, AZ 85721-0065, USA
[4] National Optical Astronomy Observatory, 950 North Cherry Avenue, Tucson, AZ 85719, USA
[5] Instituto de Astrofísica de Canarias, E-38205 La Laguna, Tenerife, Spain
[6] Departamento de Astrofísica, Universidad de La Laguna, E-38206 La Laguna, Tenerife, Spain
[7] Center for Astrophysics and Space Science, University of California San Diego, La Jolla, CA 92093, USA
[8] Department of Physics & Astronomy, Western Washington University, Bellingham, WA, 98225, USA
[9] New Mexico State University, Las Cruces, NM 88003, USA
[10] Department of Astronomy, The Ohio State University, Columbus, OH 43210, USA
[11] Materials Science and Applied Mathematics, Malmö University, SE-205 06 Malmö, Sweden
[12] Lund Observatory, Department of Astronomy and Theoretical Physics, Lund University, Box 43, SE-22100 Lund, Sweden
[13] Department of Astronomy & Astrophysics, Pennsylvania State, 525 Davey Lab, University Park, PA 16802, USA
[14] Department of Astronomy, University of Virginia, Charlottesville, VA 22904-4325, USA
[15] University of Texas at Austin, McDonald Observatory, Fort Davis, TX 79734, USA
[16] Instituto de Alta Investigación, Universidad de Tarapacá, Casilla 7D, Arica, Chile
[17] Department of Physics and Astronomy, Vanderbilt University, 6301 Stevenson Center Lane, Nashville, TN 37235, USA
[18] Department of Physics & Astronomy, Carleton College, Northfield MN, 55057, USA
[19] The Observatories of the Carnegie Institution for Science, 813 Santa Barbara Street, Pasadena, CA 91101, USA

Abstract

We present spectroscopic determinations of the effective temperatures, surface gravities, and metallicities for 21 M dwarfs observed at high resolution ($R \sim 22{,}500$) in the H band as part of the Sloan Digital Sky Survey (SDSS)-IV Apache Point Observatory Galactic Evolution Experiment (APOGEE) survey. The atmospheric parameters and metallicities are derived from spectral syntheses with 1D LTE plane-parallel MARCS models and the APOGEE atomic/molecular line list, together with up-to-date H_2O and FeH molecular line lists. Our sample range in $T_{\rm eff}$ from $\sim$3200 to 3800 K, where 11 stars are in binary systems with a warmer (FGK) primary, while the other 10 M dwarfs have interferometric radii in the literature. We define an M_{K_S}–radius calibration based on our M-dwarf radii derived from the detailed analysis of APOGEE spectra and *Gaia* DR2 distances, as well as a mass–radius relation using the spectroscopically derived surface gravities. A comparison of the derived radii with interferometric values from the literature finds that the spectroscopic radii are slightly offset toward smaller values, with $\Delta = -0.01 \pm 0.02\ R_\star/R_\odot$. In addition, the derived M-dwarf masses based upon the radii and surface gravities tend to be slightly smaller (by $\sim$5%–10%) than masses derived for M-dwarf members of eclipsing binary systems for a given stellar radius. The metallicities derived for the 11 M dwarfs in binary systems, compared to metallicities obtained for their hotter FGK main-sequence primary stars from the literature, show excellent agreement, with a mean difference of [Fe/H](M dwarf – FGK primary) = $+0.04 \pm 0.18$ dex, confirming the APOGEE metallicity scale derived here for M dwarfs.

1. Introduction

M-dwarf stars (M dwarfs) comprise roughly 70% of all stars in the Milky Way (Salpeter 1955; Miller & Scalo 1979; Henry et al. 2018). Although they represent the most numerous type of star, M dwarfs remain one of the least-studied types of stars in the Galaxy in terms of their chemical abundances. This is primarily due to their complex optical spectra that are blanketed by strong molecular bands such as TiO and VO. Interest in improving the characterization of M dwarfs in terms of stellar parameters and metallicities has increased recently as

a growing number of Earth-sized exoplanets are increasingly found orbiting M dwarfs. Small planets are easier to detect around small stars either via radial velocity (RV) or transit methods (Charbonneau & Deming 2007; Gaidos et al. 2007; Shields et al. 2016). Using data from the *Kepler* mission (Batalha et al. 2013), Dressing & Charbonneau (2015) reported that the occurrence rate of small exoplanets per M dwarf is 0.56 for Earth-sized planets (1.0–1.5 $R_\oplus$) and 0.46 for super-Earths (1.5–2.0 $R_\oplus$); see also Mulders et al. (2015).

Most of the early studies determining metallicities ([Fe/H]) in M dwarfs were based on photometric calibrations. The pioneering work of Bonfils et al. (2005) determined metallicities for a sample of 20 M dwarfs in visual binary systems

---

[20] Hubble Fellow.

containing a warmer primary of spectral type FGK. Based on the assumption that the secondary M dwarfs have the same metallicity as their primary star companions, the authors derived a calibration of M-dwarf metallicities as a function of their M_K magnitudes and $(V - K)$ colors. The works of Johnson & Apps (2009) and Schlaufman & Laughlin (2010) used similar techniques, also establishing relations between the M-dwarf metallicities and their photometric colors (see also Mann et al. 2013a; Neves et al. 2014; and Montes et al. 2018). Although obtaining M-dwarf metallicities from photometric calibrations is a significant step forward, the internal uncertainties in these measurements (generally of the order of $\sim$0.15–0.20 dex) can be an issue for detailed studies of, for example, possible planet–star connections, or the metallicity distribution of the solar neighborhood. Using spectroscopy from both high- and low-resolution spectra to derive metallicities needs to be thoroughly explored, and this can be more easily achieved in the near-IR, as the M-dwarf spectra show shallower and fewer molecular blends in the near-infrared (NIR; J, H, and K bands) than in the optical spectral regions (Allard et al. 2000; Bean et al. 2006; Quirrenbach et al. 2014; Passegger et al. 2018).

Rojas-Ayala et al. (2012) developed a technique to determine metallicities of M dwarfs from low-resolution ($R \sim 2000$) spectra in the K band (2.2 μm), using the equivalent widths (EWs) of the Na I doublet lines (2.208 and 2.261 μm), Ca I triplet lines (2.206–2.209 μm), and the H_2O–K2 index. They calibrated a metallicity scale based on 18 M dwarfs in binary systems with a warmer FGK primary companion. The works of Newton et al. (2014), Muirhead et al. (2014), Terrien et al. (2015), and Mann et al. (2013b) used similar techniques to produce spectroscopic M-dwarf metallicity calibrations based on other NIR bands or spectral lines. Veyette et al. (2016) argued that metallicity calibrations using Na I and Ca I line EW measurements may present significant uncertainties, due to the nonconsideration of CO molecular lines, which are an important source of blending in the K band (see Tsuji et al. 2015). More recently, Veyette et al. (2017) measured the EWs of Fe I and Ti I lines from high-resolution Y-band spectra of 29 M dwarfs in binary systems (with a solar-like primary companion) to produce an EW calibration for T_{eff}, [Fe/H], and [Ti/Fe], achieving an internal precision in the derived parameters that is similar to those typically achieved for FGK stars.

Going a step further, the detailed modeling of high-resolution NIR spectra of M dwarfs offers an opportunity to determine precise stellar parameters and metallicities. Önehag et al. (2012), Lindgren et al. (2016), and Lindgren & Heiter (2017) analyzed high-resolution CRIRES spectra ($R \sim 50,000$; Kaeufl et al. 2004) of a sample of M dwarfs showing that their metallicities can be derived from unblended Fe I lines in the J band (1.2 μm) via a spectral synthesis analysis. In addition, Lindgren & Heiter (2017) studied the behavior of molecular transitions of FeH, as well as atomic Fe I lines, finding that FeH lines are good indicators of effective temperature in M dwarfs. The recent work of López-Valdivia et al. (2019) used the H-band IGRINS spectra to derive atmospheric parameters of 254 K–M-dwarf stars, matching the spectra with the BT-Settl grids (Allard et al. 2013).

The high-resolution H-band spectra from the Apache Point Observatory Galactic Evolution Experiment (APOGEE; Majewski et al. 2017) survey constitute a powerful data set

to use in determining individual metallicities and detailed chemistry of M dwarfs. Souto et al. (2017) derived stellar parameters and metallicities, as well as individual abundances for 13 elements, in two early-type M dwarfs ($T_{eff} \sim 3850$ K). Souto et al. (2018) extended the same type of spectral analysis to a cooler M dwarf by deriving stellar parameters and chemical abundances (of eight species) for the mid-spectral-type exoplanet-hosting M dwarf Ross 128 ($T_{eff} \sim 3200$ K). Using APOGEE spectra as well, Rajpurohit et al. (2018) analyzed 45 M dwarfs selected from the RV study from Deshpande et al. (2013) and determined atmospheric parameters (T_{eff}, log g) and metallicities using matches to Phoenix BT-Settl spectral grids.

In this work, we analyze 21 M dwarfs with effective temperatures ranging from 3200 to 3950 K and [Fe/H] roughly from −1.00 to +0.25 dex. One of the main purposes of this study is to compare the metallicity scale of the M-dwarf spectra obtained here from the APOGEE spectra with those obtained from high-resolution optical studies of the warmer primary stars in the literature. In Section 2, we describe the stellar sample and observations, while the methodology adopted in the derivation of the atmospheric parameters and metallicities is presented in Section 3. Sections 4 and 5 are dedicated to the results and discussion, and we summarize our conclusions in Section 6.

2. Observations and Selected Sample of M Dwarfs

The studied sample is composed of 21 targets: 11 M dwarfs that are members of wide binary systems containing warmer primaries previously analyzed in the literature using high-resolution spectra (Mann et al. 2013a; Montes et al. 2018), and 10 targets that are well-studied field M dwarfs with interferometric radii measured by Boyajian et al. (2012).

The APOGEE spectra analyzed are from the Sloan Digital Sky Survey (SDSS)-IV (Blanton et al. 2017) Data Release 14 (DR14; Abolfathi et al. 2018). The original APOGEE instrument is a cryogenic high-resolution ($R = \lambda/\Delta\lambda \sim 22,500$) multifiber (300) H-band (1.51–1.69 μm) spectrograph (Wilson et al. 2010), operating on the SDSS 2.5 m telescope (Gunn et al. 2006) at Apache Point Observatory. A second instrument, virtually identical to the original one, is installed in Las Campanas Observatory, but does not concern the data employed in this work. The targets analyzed here are nearby M dwarfs having *Gaia* DR2 distances $\lesssim$80 pc (Bailer-Jones et al. 2018; Table 1). We note that two stars in our sample (2M11032023+3558117 and 2M11052903 +4331357) do not have *Gaia* DR2 parallaxes and their distances are from McDonald et al. (2017; also using parallaxes). The nearest M dwarfs in our sample ($d \sim 2.5$–7 pc) are quite bright in the H band, and these were observed with the APOGEE spectrograph fiber-fed by the 1 m telescope at the APO. The APOGEE spectra analyzed here were reduced by the ASPCAP automated pipeline, as discussed in Nidever et al. (2015) and Holtzman et al. (2018).

3. Abundance Analysis

The spectral analysis methodology adopted in this study is similar to that presented and discussed in our previous works (Souto et al. 2017, 2018). The measured spectral lines and the atomic and molecular line lists adopted in the calculations are discussed in Souto et al. (2017, 2018); we used an updated version of the DR14 APOGEE line list (described in Shetrone

Table 1
Stellar Parameters and Metallicities

2Mass ID	J	H	Ks	d (pc)	M_{K_S}	M_{bol}	$R_\star/R_\odot$	$M_\star/M_\odot$	T_{eff}	log g	A(C)	A(O)	A(Fe)	[Fe/H]
Binaries
2M03044335+6144097	8.877	8.328	8.103	23.5	6.248	8.884	0.394	0.253	3541	4.65	8.15	8.51	7.19	−0.26
2M03150093+0103083	11.622	11.043	10.855	77.5	6.408	9.029	0.352	0.254	3625	4.75	7.57	8.16	6.54	−0.91
2M03553688+5214291	10.885	10.325	10.127	39.6	7.139	9.800	0.280	0.233	3400	4.91	8.08	8.36	7.00	−0.45
2M06312373+0036445	11.077	10.465	10.252	72.1	5.962	8.564	0.412	0.325	3729	4.72	7.99	8.40	7.06	−0.39
2M08103429−1348514	8.276	7.672	7.418	20.9	5.817	8.458	0.487	0.464	3514	4.73	8.36	8.60	7.51	+0.06
2M12045611+1728119	9.793	9.183	8.967	37.6	6.091	8.756	0.458	0.505	3384	4.82	8.08	8.31	6.93	−0.52
2M14045583+0157230	10.129	9.483	9.269	51.8	5.697	8.319	0.489	0.458	3621	4.72	8.34	8.62	7.60	+0.15
2M18244689−0620311	9.659	9.052	8.795	39.6	5.807	8.473	0.524	0.589	3376	4.77	8.38	8.68	7.66	+0.21
2M20032651+2952000	9.554	9.026	8.712	16.0	7.691	10.382	0.235	0.273	3245	5.13	8.61	8.87	7.61	+0.16
2M02361535+0652191	7.333	6.793	6.574	7.2	7.287	9.962	0.271	0.245	3331	4.96	8.31	8.60	7.33	−0.12
2M05413073+5329239	6.586	5.963	5.759	12.3	5.309	7.899	0.541	0.644	3791	4.78	8.48	8.73	7.67	+0.22
Interferometric Radii
2M11032023+3558117	4.203	3.640	3.254	2.6	6.179	8.809	0.400	0.352	3576	4.78	8.07	8.43	6.99	−0.46
2M11052903+4331357	5.538	5.002	4.769	4.8	6.363	8.992	0.367	0.303	3579	4.79	8.06	8.35	6.87	−0.58
2M00182256+4401222	5.252	4.476	4.018	3.6	6.236	8.877	0.401	0.233	3517	4.60	8.17	8.38	7.02	−0.43
2M05312734-0340356	4.999	4.149	4.039	5.7	5.260	7.848	0.551	0.543	3800	4.69	8.63	8.82	7.80	+0.35
2M09142298+5241125	4.889	3.987	3.988	6.3	4.991	7.571	0.612	0.569	3846	4.62	8.25	8.52	7.62	+0.17
2M09142485+5241118	4.779	4.043	4.136	6.3	5.139	7.722	0.575	0.539	3831	4.65	8.29	8.53	7.71	+0.26
2M13454354+1453317	5.181	4.775	4.415	5.4	5.753	8.370	0.472	0.468	3641	4.76	8.21	8.52	7.21	−0.24
2M18424666+5937499	5.189	4.741	4.432	3.5	6.712	9.348	0.319	0.301	3539	4.91	8.06	8.47	6.97	−0.48
2M18424688+5937374	5.721	5.197	5.000	3.5	7.280	9.947	0.249	0.127	3371	5.00	8.16	8.65	7.00	−0.45
2M22563497+1633130	5.36	4.800	4.253	6.9	5.329	7.911	0.527	0.485	3831	4.68	8.43	8.67	7.53	+0.08

Note. The estimated uncertainties in T_{eff} and log g are 100 K, and 0.20 dex, respectively. The mean abundance uncertainties for C, O, and Fe are approximately 0.10 dex.

et al. 2015 and in V. Smith et al. 2020, in preparation, and internally labeled as 20150714), which includes the H_2O line list from Barber et al. (2006) and an FeH line list from Hargreaves et al. (2010). This is the line list adopted for the SDSS–DR16 (Ahumada et al. 2019).

We computed spectral syntheses via the semiautomated mode of the BACCHUS wrapper (Masseron et al. 2016), which uses the Turbospectrum code (Alvarez & Plez 1998 and Plez 2012) and adopted the 1D LTE (Local thermodynamical equilibrium) plane-parallel MARCS model atmospheres (Gustafsson et al. 2008). A microturbulent velocity (ξ) of 1.00 ± 0.25 km.s^{-1} was adopted for all stars (see discussion in Souto et al. 2017). Best fits between the observed and synthetic spectra were obtained via a χ-squared minimization, while we manually fixed the level of the pseudo-continuum of portions of spectra analyzed. The synthetic spectra were broadened using a Gaussian profile corresponding to the APOGEE spectral resolution ($R \sim 22{,}500$), or an FWHM of ~ 0.73 Å. Such resolution imposes a threshold of ~ 7 km s^{-1} in the detection of the stellar projected rotational velocity, $v \sin i$. Most of the targets had very low values of $v \sin i$ that could not be measured, except for two stars that had detectable $v \sin i$ above this threshold: 2M12045611+1728119, with $v \sin i = 13.5 \pm 2.0$ km.s^{-1}, and 2M18244689–0620311, with $v \sin i = 10.0 \pm 2.0$ km.s^{-1}.

3.1. Atmospheric Parameters and Metallicities

To estimate the effective temperature of a studied M dwarf, we derived the oxygen abundances from H_2O and OH lines for a set of effective temperatures, T_{eff}, ranging from 3200 to 4300 K in steps of 100 K. As the OH and H_2O lines have different sensitivities to T_{eff} (the OH lines are not very sensitive to T_{eff}, while the H_2O lines are), there is a unique solution for

T_{eff} that yields the same oxygen abundance from both OH and H_2O lines; this is defined by one T_{eff}–A(O) pair. In this analysis, we initially adopt a log $g = 4.75$.

It should be kept in mind, however, that the derived O abundance is dependent on the C abundance, as expected due to the important role that CO molecules play in the molecular equilibrium pressures. For C/O < 1 (which is expected for all M dwarfs), C in the stellar atmospheres will tend to be bound in CO, with the remaining O then bound to OH. (This behavior is different for stars with C/O > 1). For a given T_{eff}, the CO lines in the APOGEE spectra effectively define the carbon abundance of the star, with almost no dependency on the oxygen abundance. We determine the carbon abundance from fits to the CO lines; we used two CO lines at $\lambda = 15978$ and 16185 Å, which are well defined in the spectra of M dwarfs. The derived [C/Fe] and [O/Fe] abundances for the studied M dwarfs, which are in the solar neighborhood, are overall consistent with the expected behavior from chemical evolution. For the most metal-poor star in our sample ([Fe/H] = −0.9), the oxygen abundance is found to be enhanced ([O/Fe] = +0.41). The C and O abundances will be discussed in full detail in a future paper (D. Souto et al. 2020, in preparation) where the abundances for 11 other chemical elements will also be presented.

We present an example of a T_{eff}–A(O) diagram in the top panel of Figure 1. The dashed line connects the oxygen abundances from H_2O lines, while the solid line connects the oxygen abundances from OH lines; changes in T_{eff} of 100 K result in oxygen abundance differences of about ~ 0.10 dex from H_2O lines, while we obtain abundance changes less than ~ 0.02 dex using the OH lines. The top-left and top-middle panels of Figure 1 show spectral regions dominated by H_2O
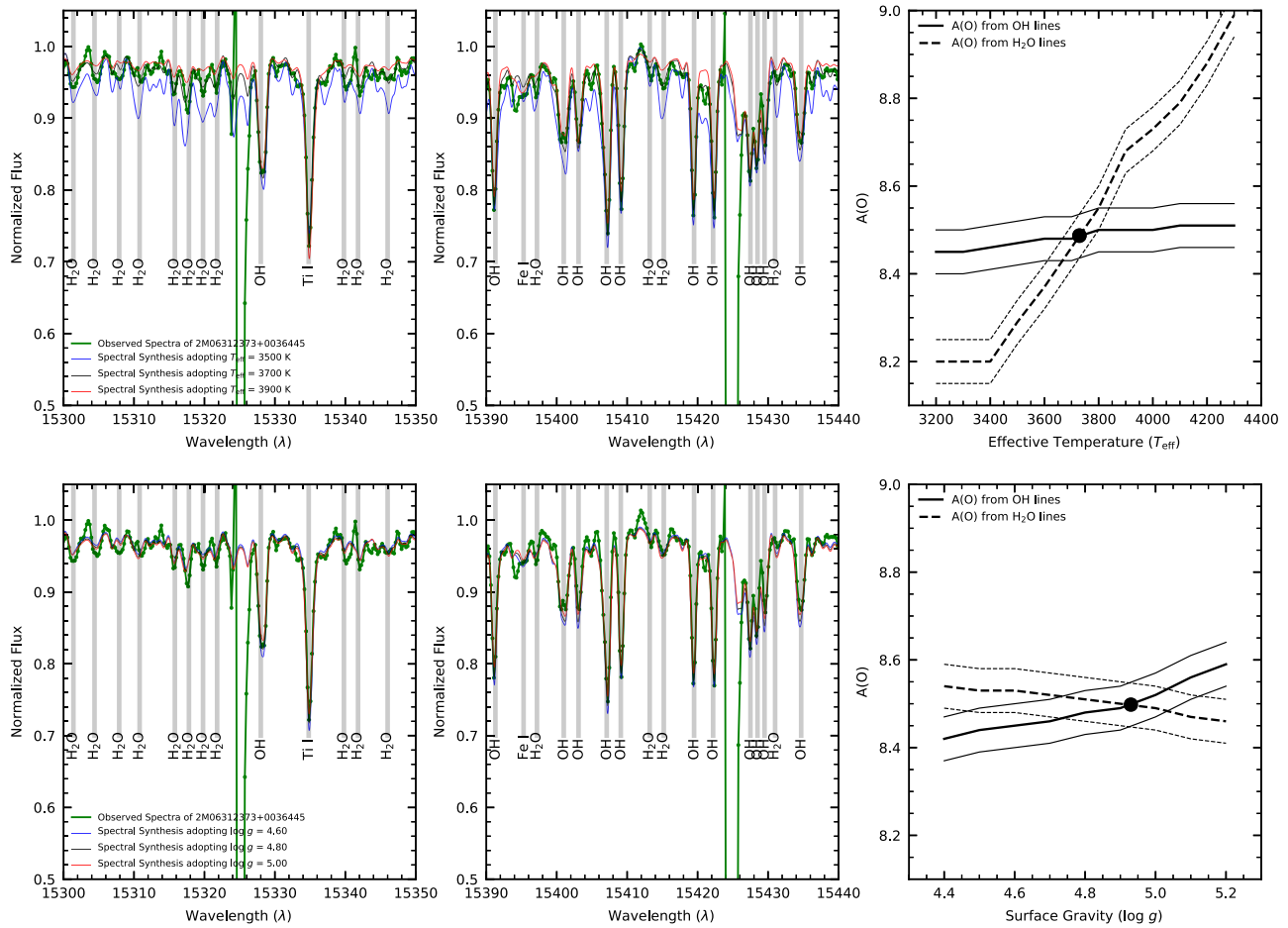
Figure 1. Top and bottom left and middle panels: portions of the APOGEE spectrum of the M dwarf 2M06312373+0036445 are shown as green dotted lines. Spectral syntheses computed assuming $T_{\rm eff}$ = 3500, 3700, and 3900 K (log g = 4.8; top panel) and assuming log g = 4.6, 4.8, and 5.0 ($T_{\rm eff}$ = 3729 K; bottom panel) are shown as blue, black, and red solid lines, respectively. Right panels: the abundance of oxygen from OH and H_2O lines as a function of $T_{\rm eff}$ (top) and as a function of log g (bottom). The filled circles represent the pairs $T_{\rm eff}$–A(O) and log g–A(O) that indicate an agreement between the abundance indicators.

and OH lines, respectively. The observed spectrum of the sample M dwarf 2M06312373+0036445 is shown as a dotted green line. To illustrate the sensitivity of the H_2O and OH lines to changes in the adopted $T_{\rm eff}$, we overplot synthetic spectra for $T_{\rm eff}$ = 3500 (blue line), 3700 (black line), and 3900 K (red line). It is clear that the H_2O lines are the most sensitive to $T_{\rm eff}$ when compared to the other spectral lines in the region, in particular, to the OH lines.

Spectroscopic log g are obtained from the log g–A(O) pair. The method used to determine the log g is similar to the one adopted for the effective temperature. However, instead of changing the $T_{\rm eff}$, we now vary the log g (we test log g from 4.4 to 5.2 dex in steps of 0.10 dex), deriving oxygen abundances with the log g that produce consistent solutions. In the bottom panel of Figure 1, we present the log g–A(O) pair in the same format as in top panel. The OH lines are more sensitive to changes in log g than $T_{\rm eff}$, while the oxygen abundances derived from the H_2O lines now decrease as log g increases. This method is limited in $T_{\rm eff}$ as the H_2O lines become very weak in hotter M dwarfs, with an effective temperature above $T_{\rm eff} \sim$ 3950 K and, therefore, this methodology cannot be applied to such warm dwarfs.

We note that such sensitivity plots (as shown in Figure 1) can also be constructed using Fe I and FeH lines. In the present study, we also investigated consistent solutions for $T_{\rm eff}$ and log

g using four spectroscopic indicators: OH and H_2O lines along with Fe I and FeH lines. However, the effective temperatures and surface gravities derived using Fe I and FeH exhibited small systematics: hotter effective temperatures when compared to fundamental $T_{\rm eff}$ from angular diameters (on average by $\sim$150 K), as well as lower surface gravities than expected for a cool main-sequence star (on average by $\sim$0.15 dex). These systematics could result from more considerable uncertainties in the gf values of the FeH transitions in our line list (V. Smith et al. 2020, in preparation); thus, FeH lines were not considered here in deriving this work's stellar parameters. Nonetheless, deriving the iron abundances only from adjusting the Fe I line profiles, we still find reasonable consistency with the FeH line abundances at the level of $\sim$0.10–0.20 dex.

Figure 2 presents a comparison of the iron abundances derived from Fe I and FeH transitions; the bottom panel in this figure displays the residual abundance difference between these two indicators. The difference between these two metallicity indicators is $\langle$[Fe I/H] − [FeH/H]$\rangle$ = +0.12 ± 0.10 dex. We note that this result is in line with the previous finding from Souto et al. (2017), who obtained a systematic difference of 0.10–0.15 dex in the Fe abundances from Fe I and FeH in two M dwarfs.
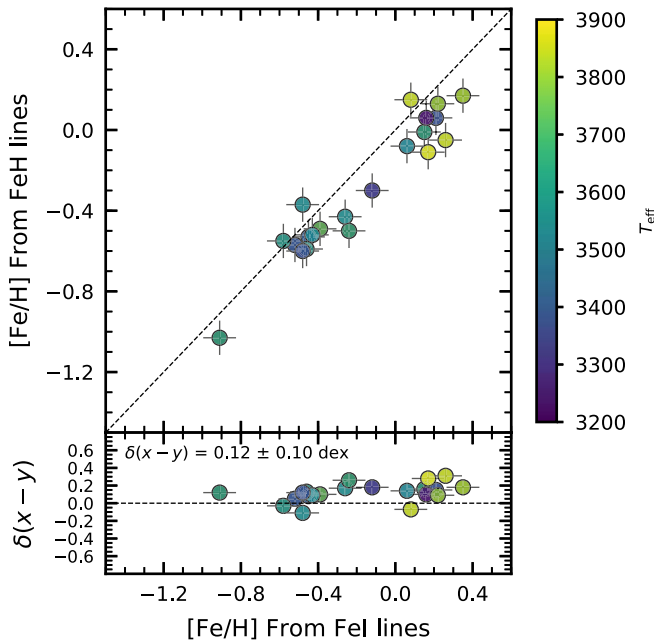
Figure 2. The comparison between the iron abundances obtained from the FeH molecular lines and the atomic Fe I lines. The results are color coded by effective temperature. The difference between these two metallicity indicators is $\langle$[Fe I/H] $-$ [FeH/H]$\rangle = +0.12 \pm 0.10$ dex. The residual (x–y) diagram is shown at the bottom panel.

3.2. Stellar Radii and Masses

Radii for the M dwarfs analyzed here were calculated using the definition of luminosity ($L_\star$),

$$R_\star = \left(\frac{L_\star}{4\pi\sigma T_{\mathrm{eff}}^4}\right)^{1/2}, \qquad (1)$$

where the effective temperatures used in Equation (1) were those derived here spectroscopically. Luminosities for 16 of the targets were computed directly from the measured bolometric fluxes at Earth, F_{bol}, presented in Mann et al. (2015), combined with the accurate distances from Bailer-Jones et al. (2018), which are based on *Gaia* DR2 (Table 1), assuming no interstellar extinction. Five stars in our sample did not have measured values of F_{bol}, so we used their absolute Ks-band magnitudes, M_K, along with Ks-band bolometric corrections to derive M_{bol} and then $L_\star$ using

$$L_\star = L_0 10^{-0.4*M_{\mathrm{bol}}}. \qquad (2)$$

We used the recommended values from Mamajek et al. (2015) of $M_{\mathrm{bol}} = 0.00$ corresponding to $L_0 = 3.0128 \times 10^{35}$ erg s^{-1}, which leads to the solar luminosity of 3.828×10^{33} erg s^{-1} and $M_{\mathrm{bol}}(\mathrm{Sun}) = 4.74$. Ks-band bolometric corrections for these five M dwarfs were derived by using the 16 stars with directly measured luminosities to determine their individual Ks-band bolometric corrections from $BC_K = M_{\mathrm{bol}} - M_K$. These values of BC_K define a tight relation of BC_K with our derived T_{eff}. The five M dwarfs without measured values of F_{bol} span a range in T_{eff} of 3400 K–3800 K, and over this temperature range, a linear relation of BC_K with T_{eff} results in a good fit, with $BC_K = (3.287 - 1.839) \times 10^{-4} \times T_{\mathrm{eff}}$. Differences between the values of BC_K compared to the linear fit values result in a mean

difference of $\Delta = 0.00 \pm 0.03$ mag, or ~ 0.03 in $L_\star$, and an error in $R_\star \sim 1.5\%$.

Given the derived radii, stellar masses can then be inferred from the fundamental relation

$$M = gR^2/G. \qquad (3)$$

3.3. Estimated Uncertainties

The uncertainties in the determinations have been discussed in detail in previous studies, and we refer to the abundance sensitivities presented in Table 4 of Souto et al. (2017) and Table 2 of Souto et al. (2018). The latter studies estimate that the typical uncertainties in the iron and oxygen abundances are about ~ 0.1 dex for a change of 65 K in T_{eff}, 0.10 dex in log g, 0.2 in the [M/H] of the model atmosphere, and $+0.25$ km s^{-1} in the microturbulent velocity. We estimate that the typical uncertainties in the iron and oxygen abundances are about ~ 0.1 dex for a change of ~ 100 K in T_{eff}, 0.2 dex in log g, 0.2 in the [M/H] of the model atmosphere, and $+0.25$ km s^{-1} in the microturbulent velocity.

If we assume that $\delta(A(\mathrm{OH}) - A(\mathrm{H_2O}))$ can differ by up ± 0.10 dex (which is the typical measurement precision) as shown by the uncertainty lines in the diagram of O abundances as a function of T_{eff} and log g; Figure 1), we obtain the typical uncertainty in T_{eff} to be ± 100 K. Using the same procedure for estimating the uncertainties in log g, we obtain the uncertainty to be $\sigma(\log g) \sim 0.20$ dex.

To determine the errors in the derived stellar radii, we adopt the same procedure as Martinez et al. (2019) and propagate the mean associated errors in the Ks band (0.022 mag; Skrutskie et al. 2006), distances (~ 0.15 pc), and T_{eff} (~ 100 Kl the variables in Equation (1)). We obtain the errors in our stellar radii to be about 5% total in $R_\star/R_\odot$, or $\sim 0.023 R_\star/R_\odot$ We ignore errors due to extinction and note that that we did not use any reddening for our targets.

4. Results

The atmospheric parameters, metallicities, radii, and masses for our sample of 21 M dwarfs are presented in Table 1. These results will be used in the future to calibrate the APOGEE automated pipeline (ASPCAP; García Pérez et al. 2016) to produce improvements in the abundances of the M dwarfs observed in the APOGEE survey.

The results from this study can be compared to those from previous studies using complementary techniques. Such comparisons can provide insights into the uncertainties and possible systematic effects inherent in the various analysis methods, as well as improved understanding of differences with theoretical stellar models. Reviewing the results obtained from different quantitative analysis techniques, along with the predictions/results from models, is a useful and particularly timely endeavor, given the increased observational efforts dedicated to M dwarfs as exoplanet host stars.

4.1. Comparisons with Models

In Figure 3 (top panel), we show the Kiel diagram (T_{eff}–log g) showing the results for stellar parameters in this study. The color bar represents the stellar metallicity of the stars, and we also show as a reference the solar age–metallicity isochrone (4.5 Gyr and [Fe/H] = 0.00) from Baraffe et al. (2015; black dashed line), as well as three solar metallicity isochrones from
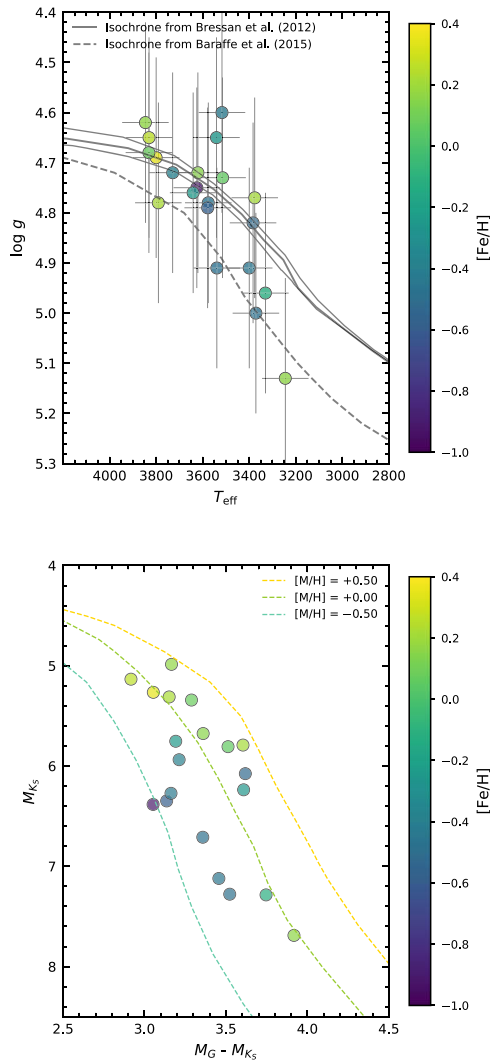
Figure 3. Top panel: the Kiel diagram showing the derived stellar parameters for the stars in this study. We also show a solar age–metallicity isochrone (4.5 Gyr and [Fe/H] = 0.00) from Baraffe et al. (2015) and three solar metallicity isochrones from Bressan et al. (2012) corresponding to 1.0, 4.5, and 10.0 Gyr. Bottom panel: the color–magnitude diagram based on *Gaia* (Gaia Collaboration et al. 2018) and 2MASS magnitudes. The dashed-line isochrones are from Bressan et al. (2012). The color bars indicate the derived metallicities for the M dwarfs.

Bressan et al. (2012) corresponding to 1.0, 4.5, and 10.0 Gyr (black solid lines; PARSEC isochrones). Overall, the derived $T_{\rm eff}$ and log g for the M dwarfs fall mostly between the two sets of isochrones with some scatter, and perhaps a tendency for the two coolest M dwarfs in our sample follow more closely the Baraffe et al. (2015) isochrone, while the PARSEC isochrone may better describe the hottest M dwarfs in our sample. In the bottom panel of Figure 3, we show the color–magnitude diagram with absolute magnitudes from *Gaia* (Gaia Collaboration et al. 2018) and the Two Micron All Sky Survey (2MASS) catalog. For guidance, we also plot three dashed lines representing PARSEC isochrones assuming different metallicities: +0.50 (yellow), 0.00 (green), and −0.50 (blue) dex. The M dwarfs with near-solar metallicities generally track the solar metallicity isochrone, while the more metal-poor M dwarfs are displaced and tend to follow the more metal-poor isochrone. The overall consistent behavior, within the uncertainties, of our purely spectroscopically derived $T_{\rm eff}$ and log g results when compared

to models in the Kiel diagram, as well the comparison of the stellar metallicities and the models in the color–magnitude diagram, reinforces the general consistency between our spectroscopic results and the models. However, a detailed comparison indicates that, as expected, there is room for improvements that could be achieved both on the modeling and on the observational sides.

4.2. Comparisons with the Literature

4.2.1. Effective Temperatures

The target stars have been well studied in the literature; here we compare our effective temperatures for M dwarfs in common with the works of Rojas-Ayala et al. (2012), Mann et al. (2015), and with the fundamental $T_{\rm eff}$ from Boyajian et al. (2012).

As mentioned previously, 10 target stars are in common with the Boyajian et al. (2012) study, all having fundamental effective temperatures obtained from direct measurements of angular diameters using the interferometric CHARA array. Boyajian et al. (2012) derived the stellar radius, R, using the trigonometric relation $\theta_{\rm LD} = 2R/d$, where θ is the measured angular diameter and d is the stellar distance obtained from the *Hipparcos* parallax (van Leeuwen 2007), and obtained effective temperatures using the flux–luminosity definition: $T_{\rm eff} = 2341$ $(F_{\rm bol}/\theta_{\rm LD}^2)^{1/4}$, where $F_{\rm bol}$ is in units of 10^{-8} erg cm^{-2} s^{-1} (where $F_{\rm bol}$ is from Boyajian et al. 2012) and $\theta_{\rm LD}$ is in milliarcseconds. In this study, we also derived the stellar radii and fundamental effective temperatures using the same angular diameter measurements from Boyajian et al. (2012), but we now adopt more precise *Gaia* DR2 distances from Bailer-Jones et al. (2018) and bolometric fluxes from Mann et al. (2015).

The comparison of the results is presented in Figure 4 (left panel); a residual diagram is displayed at the bottom of the figure and the results are color coded by metallicity. The circle and triangle symbols represent the fundamental $T_{\rm eff}$ taken directly from Boyajian et al. (2012) and the fundamental $T_{\rm eff}$ computed in this study using the Boyajian et al. (2012) angular diameters, respectively. There is a small systematic offset in the sense that our spectroscopic $T_{\rm eff}$ are hotter than the fundamental ones: $\langle T_{\rm eff}({\rm this\ work}) - T_{\rm eff}\ ({\rm fundamental;\ Boyajian\ et\ al.}$ 2012)$\rangle = +56 \pm 101$ K; while using the angular measurements together with more precise distances from Bailer-Jones et al. (2018) we obtain $\langle T_{\rm eff}({\rm this\ work}) - T_{\rm eff}({\rm fundamental;\ this}$ work)$\rangle = +32 \pm 105$ K, indicating a better agreement in the comparison. We note, however, that one star deviates significantly from perfect agreement, which is also the coolest one in the comparison (2M18424688+5937374; [Fe/H] = −0.45). From the spectroscopic analysis of APOGEE spectra presented here, we obtain $T_{\rm eff} = 3371$ K, while using the angular diameter from Boyajian et al. (2012) and the *Gaia* DR2 distance, we obtain $T_{\rm eff} = 3106$ K, resulting in a $\delta T_{\rm eff}$ of approximately 250 K. In Figure 5, we show for comparison two synthetic spectra, one corresponding to the stellar parameters obtained here from the APOGEE spectra and another for the $T_{\rm eff}$ obtained from the Boyajian et al. (2012) angular diameter d (adopting log $g = 5.00$). It is clear that $T_{\rm eff}$ around 3100 K is too low and does not fit well the APOGEE spectrum for the star 2M18424688+5937374 (shown as a dashed black line in Figure 5). The effective temperature derived in this study of 3371 K is, however, in good agreement with an average of the effective temperatures for this star, $\langle T_{\rm eff} \rangle = 3310 \pm 87$ K,
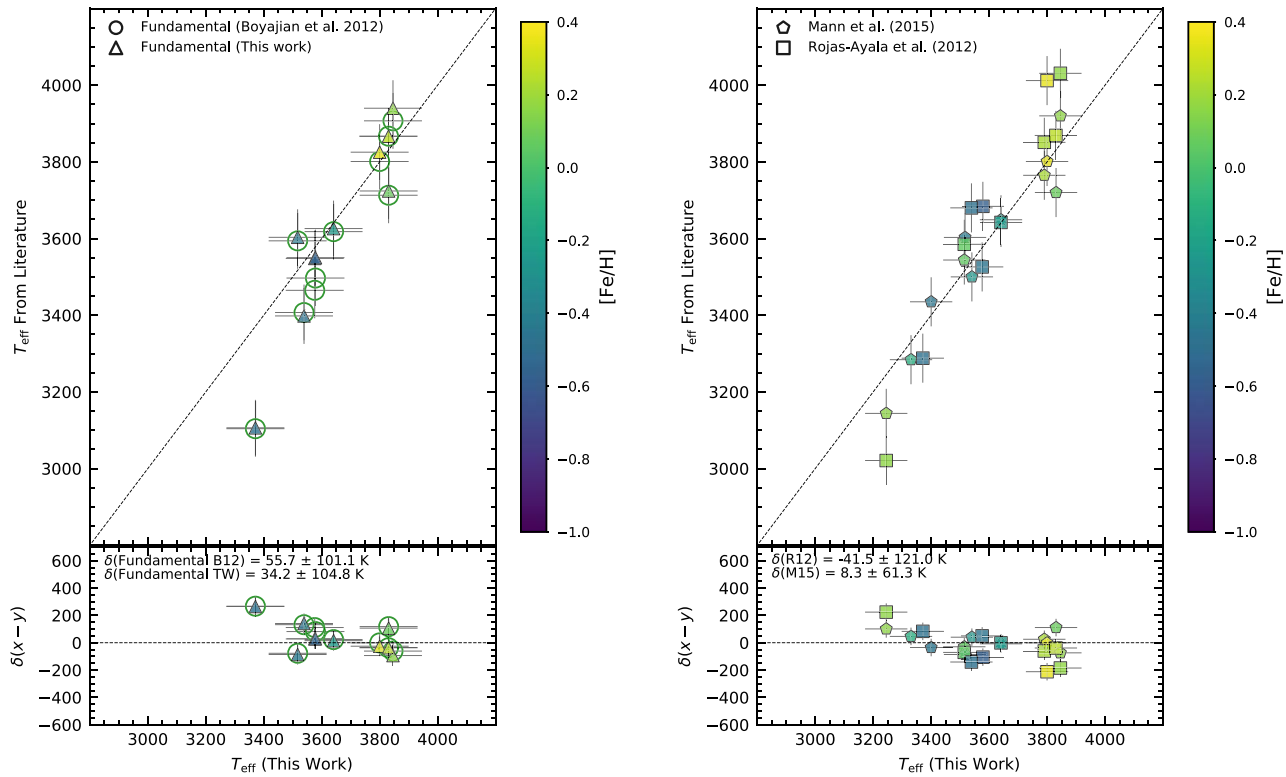
Figure 4. The comparison between the effective temperatures from the APOGEE spectra derived in this study and those from the fundamental scale based on measurements of angular diameters (left panel) and other studies in the literature (right panel). Results are color coded by the metallicity.

obtained from the literature (Valenti et al. 1998; Rojas-Ayala et al. 2012; Lepine & Gaidos 2013; Gaidos et al. 2014; Gaidos & Mann 2014; Mann et al. 2015). It is worth pointing out that interferometric measurements are not completely free from systematic issues, for example, only a fraction of the visibility curve is measured for this star given the small stellar angular size (see Figure 3 in Boyajian et al. 2012). If we remove this star from the comparison, we obtain $T_{\rm eff}$(this work) − $T_{\rm eff}$(fundamental; this work)⟩ = +8 ± 75 K, which represents significantly better agreement (or, $\delta = -42 \pm 121$ K assuming directly the effective temperatures from Boyajian et al. 2012).

Rojas-Ayala et al. (2012) used low-resolution Ks-band spectra of a sample of M dwarfs with effective temperatures derived from the H_2O–K2 index (Covey et al. 2010). Mann et al. (2015) also used low resolution, but optical and near-infrared, spectroscopy to determine effective temperatures from best matches between their optical spectra and a synthetic grid from BT-Settl Phoenix models (Allard et al. 2013). Our effective temperatures, which are based upon APOGEE spectra, present reasonably good agreement with the results from the works mentioned above, as can be seen in Figure 4 (right panel, same format as the left panel), but there are differences and/or discrepant points both at the low and high effective temperature end and a possible small dependence on the effective temperature, as can be seen from the bottom panel of this figure. The comparison with results from Mann et al. (2015) shows no offset and a small rms: ⟨$T_{\rm eff}$(this work) − $T_{\rm eff}$ (Mann et al. 2015⟩ = +8 ± 61 K. When comparing to Rojas-Ayala et al. (2012), our $T_{\rm eff}$ are slightly lower with a relatively larger scatter: ⟨$T_{\rm eff}$(this work) − $T_{\rm eff}$(Rojas-Ayala et al. 2012)⟩ = −29 ± 139 K.

4.2.2. Stellar Metallicities

We compiled metallicity results for the M dwarfs studied in other works in the literature. In Figure 6 (top panel), we present the comparison of the derived metallicities with results from the following studies: Rojas-Ayala et al. (2012), Mann et al. (2013a, 2015), Newton et al. (2014), Gaidos & Mann (2014), Gaidos et al. (2014), Terrien et al. (2015), Veyette et al. (2017), and Schweitzer et al. (2019). The top panel of Figure 6 reveals an overall good agreement between the metallicity results, although the Fe abundances derived here for the metal-rich sample ([Fe/H] > 0.00) tend to lie above the abundances derived from the other studies, but not all of them. We computed an average of the metallicity values available from the literature for each star, and a comparison with our results (color coded by the effective temperature) is shown in the bottom panel of Figure 6. The mean difference between the metallicities in this case is ⟨[Fe/H](this work) − ⟨[Fe/H] (literature)⟩⟩ = 0.00 ± 0.19 dex.

4.2.3. Stellar Radii

The comparison of the M-dwarf radii obtained in this work with the interferometric radii reported in Boyajian et al. (2012) and computed in this study using $Gaia$ DR2 distances (Section 4.2.1) is presented in Figure 7 as a function of the derived effective temperatures (indicated by the color bar). There is good agreement between the scales with a slight radius dependence that can be seen in the bottom panel of the figure showing $\delta R_\star / R_\odot$ versus $R_\star / R_\odot$. As discussed previously for the effective temperature comparison, the slight radius dependence is basically due to one star, or a single interferometric measurement, notably for the lowest-mass/smallest object in our sample, where only a fraction of the
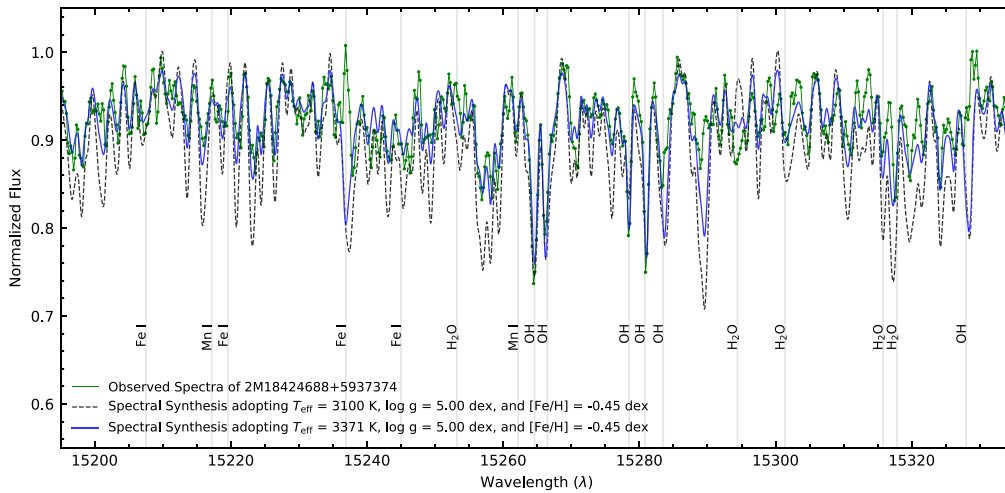
Figure 5. A portion of the APOGEE spectra displaying the observed spectrum of 2M18424688+5937374 in green. Two spectral syntheses computed with $T_{eff} = 3100$ and 3371 K (in both cases with $\log g = 5.00$ dex and [Fe/H] $= -0.45$ dex) are shown in dashed black and solid blue lines, respectively.

visibility curve is measured because of its small angular size. The mean difference between the radii shows just an insignificant offset: $\langle \delta(\text{this work–Boyajian et al. } 2012)\rangle = -0.01 \pm 0.03 R_\star / R_\odot$, while using new distances we obtain $\delta = -0.01 \pm 0.02 R_\star / R_\odot$.

Stellar radii measured from interferometry are certainly the reference scale in this comparison, for example, the uncertainties in the measured radii in Boyajian et al. (2012) are estimated to be less than about 1% (smaller than the symbol size in Figure 7), although it is always possible that the measured radii from interferometry may not be completely free from systematics as previously mentioned. The estimated errors in our derived radii are larger (5%) and given the uncertainties, we can conclude that there is reasonable consistency between the $R_\star/R_\odot$ scales.

4.3. Comparisons with Photometric Scales for M Dwarfs

Besides doing direct comparisons for M dwarfs in common with other studies, it is also of interest to apply photometric calibrations from the literature to estimate effective temperatures for our M-dwarf sample. Here we will adopt the photometric $V - J$, $r - J$, $V - H$, and $V - K_s$ calibrations from Mann et al. (2015) and Boyajian et al. (2012, discussed in the previous section) and, in addition, the one by Casagrande et al. (2008), based on a modified version of the InfraRed Flux Method (Blackwell et al. 1979) with Phoenix model atmospheres. The stellar V, J, H, and K_s magnitudes for the stars are taken from the UCAC4 (Zacharias et al. 2013) and 2MASS (Skrutskie et al. 2006) catalogs, and no reddening correction is considered. Overall, the photometric temperature scales are systematically lower than the one derived here from APOGEE spectra; the Mann et al. (2015) T_{eff} scale falls closer to our scale than the Boyajian et al. (2012) or Casagrande et al. (2008) one, which also exhibit somewhat larger scatter. The mean differences (and standard deviation) are $\langle T_{eff}(\text{this work}) - T_{eff}(\text{Mann})\rangle = +46 \pm 90$ K; $\langle T_{eff}(\text{this work}) - T_{eff}(\text{Boyajian})\rangle = +85 \pm 113$ K; and $\langle T_{eff}(\text{this work})-T_{eff}(\text{Casagrande})\rangle = +177 \pm 117$ K. Systematic differences between spectroscopic and photometric T_{eff} were previously reported in, e.g., Casagrande et al. (2008), Önehag et al. (2012), Mann et al. (2015), and Schmidt et al. (2016). Schmidt et al. (2016) adopted effective temperatures determined automatically from the APOGEE SDSS-III Data

Release 12 (DR12; Eisenstein et al. 2011; Alam et al. 2015). We note that the effective temperatures reported in DR12 are not as accurate in the form as those here, due to the lack of H_2O and FeH line lists.
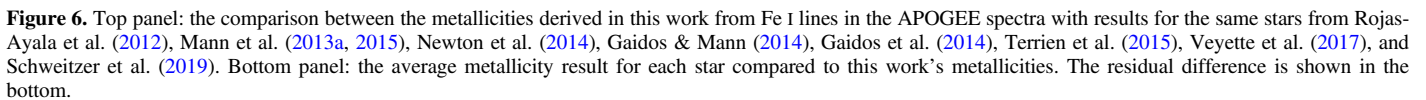
Clear trends and significant scatter in the δT_{eff} (this work—photometric) as a function of [Fe/H] can be seen in Figure 8 for the photometric scales by Mann et al. (2015, left panel), Boyajian et al. (2012, middle panel), and Casagrande et al. (2008, right panel); in each case, we show (as a black line) a linear regression to δT_{eff}–[Fe/H]. The T_{eff} differences with the Mann et al. (2015) calibration show the smallest trend as a function of metallicity. For the Casagrande et al. (2008) calibration, we observe a significant trend, where metal-rich stars display systematically lower T_{eff} than the ones derived in this study, while the opposite trend (although smaller) is observed using the Boyajian et al. (2012) calibration.

5. Discussion

The quantitative analysis of the APOGEE high-resolution NIR spectra presented in Section 3 can be used to derive purely spectroscopic fundamental stellar parameters: T_{eff}, $\log g$, and [Fe/H]. Without the need for photometric relations for T_{eff} or $\log g$, our analysis provides an independent method to determine atmospheric parameters and metallicities based on high-resolution spectroscopy that yields independent stellar radii and masses. These can then be compared to the same quantities derived from other observational techniques or predictions from models, and to the fundamental radii and masses obtained from low-mass M-dwarf eclipsing binary systems.

5.1. Fundamental Parameters of M Dwarfs

The stellar mass–radius relation obtained in this study is shown in Figure 9. The derived radii and masses (represented by green circles) are from the spectroscopic results in this study and from fundamental relations (Section 3.2). Polynomial fits to the data are also shown in the figure as solid and dashed lines, corresponding to first-degree and second-degree polynomial fits, respectively. The second-degree polynomial fit is

Figure 6. Top panel: the comparison between the metallicities derived in this work from Fe I lines in the APOGEE spectra with results for the same stars from Rojas-Ayala et al. (2012), Mann et al. (2013a, 2015), Newton et al. (2014), Gaidos & Mann (2014), Gaidos et al. (2014), Terrien et al. (2015), Veyette et al. (2017), and Schweitzer et al. (2019). Bottom panel: the average metallicity result for each star compared to this work's metallicities. The residual difference is shown in the bottom.

(green dashed line):

$$M_\star/M_\odot = 0.2524 - 0.5765(R_\star/R_\odot) + 2.0122(R_\star/R_\odot)^2,$$

(4)

which has an rms = 0.067, while a linear (first-degree) fit is quite similar (solid green line), with a slope and intercept of −0.0760 and 1.107, with an rms of 0.078. We estimate that the uncertainty in log g dominates the total uncertainty and creates most of the scatter observed in the relation of $M_\star$ as a function of $R_\star$. We note that the discrepant point that falls off the relation as having too large a mass for its radius is 2M12045611+1728119, which was discussed in Section 3 as

being one of two stars in this sample with a measurable rotational velocity, with $v \sin i = 13.5$ km s^{-1} (the largest $v \sin i$ in this sample).

A "gold standard" against which to compare the mass–radius relation derived here is the mass–radius relation deduced from the analysis of low-mass M-dwarf eclipsing binary systems; results from such systems (from Torres & Ribas 2002; Ribas 2003; López-Morales & Ribas 2005; Irwin et al. 2009, 2011, 2018; Morales et al. 2009a, 2009b; Carter et al. 2011; Doyle et al. 2011; Kraus et al. 2011; Bass et al. 2012; Hełminiak et al. 2012; Orosz et al. 2012a, 2012b; Torres et al. 2018, and Iglesias-Marzoa et al. 2019) are also shown in Figure 9 as black crosses, along with first- and second-degree
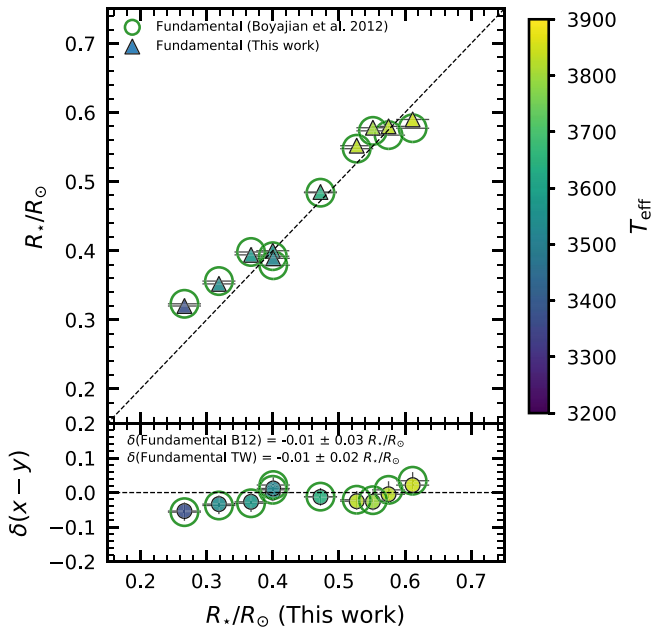
Figure 7. The comparison between the derived stellar radii with those measured from interferometry and *Hipparcos* distances in Boyajian et al. (2012) and those computed in this work using *Gaia* DR2 distances.

polynomial fits to these data. The mass–radius relation for the eclipsing binary stars exhibits very small scatter. The relation for the eclipsing binaries (shown as black solid and dashed curves, respectively) have the following coefficients: $a_0 = -0.0203$, $a_1 = 1.046$, and an rms $= 0.018$ for a first-degree fit, and $a_0 = -0.14491$, a_1 1.67400, and $a_2 = -0.70526$, with rms $= 0.011$ for a second-degree fit.

The APOGEE spectroscopic results for mass–radius can be compared to those derived from the eclipsing binary M dwarfs and exhibit a small but measurable offset (as can be seen in Figure 9), with the spectroscopic results falling below the relation based on dynamical studies of the eclipsing binary stars. The polynomial fits can be compared directly and yield differences of $\Delta(M_\star/M_\odot)$ (this study—eclipsing binaries) $= -0.01$ at $0.2\,M_\odot$ (or 5%), -0.03 at $0.3\,M_\odot$ (10%), -0.04 at $0.4\,M_\odot$ (10%), -0.04 at $0.5\,M_\odot$ (8%), and -0.04 at $0.6\,M_\odot$ (7%). These differences are not large, and our suspicion is that much of them may reside in uncertainties in the spectroscopic derivation of log g.

The relation between the absolute K magnitude, M_{K_S}, as a function of stellar radius is shown in Figure 10. Also shown are two fits to the data, where the solid and dashed lines represent first- and second-degree polynomials, respectively,

$$R_\star / R_\odot = \sum_{n=0}^{n} a_n (M_{K_S})^n. \qquad (5)$$

The coefficients obtained for the second-degree polynomial fit to the data are $a_0 = 1.9932$, $a_1 = -0.3659$, and $a_2 = 0.0177$ (with an rms scatter of 0.008), and for the first-degree polynomial fit we obtained $a_0 = 1.3024$, and $a_1 = -0.1431$ (with an rms scatter of 0.010). It has been reported previously in the literature that there is a small dependence on metallicity in the M_{K_S}–radius relation (Mann et al. 2015) and that this dependence becomes more important in the metallicity range between [Fe/H] -1.0 and -2.0 (Kesseli et al. 2019). Our

M-dwarf sample covers metallicities between roughly -1 and $+0.3$ dex, and we investigate the metallicity dependency in the M_{K_S}–radius relation by performing a fit to the data that includes the stellar metallicity as a second independent variable $(1 + b$ ([Fe/H])). A second-degree polynomial fit results in coefficients of $a_0 = 1.1621$, $a_1 = -0.1069$, $a_2 = -0.0020$, and $b = 0.1182$. We obtain $a_0 = 1.2419$, $a_1 = -0.1321$, and $b = 0.1118$, for a first-degree polynomial best fit.

The inclusion of a metallicity term in the second-order polynomial fit results in a small improvement in the residuals (rms $= 0.008$ and 0.007 for second- and first-order polynomial fits, respectively). We note that in all cases, the relations are valid for M dwarfs with M_{K_S} in the range of 5.14–7.52.

As discussed in Mann et al. (2015), the errors in the radius and the absolute magnitudes, M_{K_S}, are correlated, as these two quantities depend on the adopted distances and their uncertainties. Propagating the uncertainties into the M_{K_S}–$R_\star/R_\odot$ relation results in an internal uncertainty of $0.03 R_\star/R_\odot$. We adopted the errors in the magnitude to be ~0.022 mag, distances $= 0.15$ pc, [Fe/H] $= 0.10$ dex, $T_{\rm eff} = 100$ K, and in our derived values of $R_\star/R_\odot = 0.023$.

We note that the two stars in Figure 10 having significantly larger radii at their respective absolute K magnitudes are 2M12045611+1728119 ($M_{K_S} = 6.076$ and $R_\star/R_\odot = 0.458$), and 2M18244689–0620311 ($M_{K_S} = 5.791$ and $R_\star/R_\odot = 0.524$), which are the two M dwarfs in this sample with detectable rotational velocities ($v \sin i = 13.5$ and 10.0 km s^{-1}, respectively). As rotation and magnetic activity are correlated in late-type (FGKM) dwarfs (e.g., Suárez Mascareño et al. 2016), these two more rapidly rotating M dwarfs quite possibly are more magnetically active than the other M dwarfs in this sample. It has been suggested that the radii of magnetically active, cool, convective dwarf stars (such as M dwarfs) might be inflated due to magnetic inhibition of convection (e.g., Mullan & MacDonald 2001 or Feiden & Chaboyer 2014), or by dark star spots blocking emergent flux (e.g., MacDonald & Mullan 2013), or a combination of both effects. For example, Jackson et al. (2018) have recently measured "inflated" radii (by about 14%) in magnetically active Pleiades M dwarfs. The larger radii of 2M12045611+1728119 and 2M18244689–0620311 may be related causally to their rapid rotation.

5.2. The Metallicity Scale: M Dwarfs in Binary Systems

It is reasonable to assume that in a binary system, the primary star shares the same (or nearly the same) metallicity and chemical composition as the secondary star. The M-dwarf metallicity scale derived here from the APOGEE spectra of 11 M dwarfs, which are secondary stars in binary systems having warmer companions as primaries, can be checked against the well-defined metallicities of the warmer primaries to search for systematic differences and, ultimately, to serve as an additional validation of the M-dwarf metallicity scale in this study.

We searched the literature for high-resolution spectroscopic studies that previously measured metallicities of the primary stars in our sample. Table 2 presents the adopted metallicities for the primaries, which were taken from the following high-resolution works in the literature: Adibekyan et al. (2012), Ammons et al. (2006), Bensby et al. (2014), Carretta et al. (2013), De Silva et al. (2015), Ghezzi et al. (2010), Lambert & Reddy (2004), Mann et al. (2013a), Mishenina et al. (2008), Reddy et al. (2006), and Ramírez et al. (2007, 2012). When more than one metallicity value was available, we averaged the
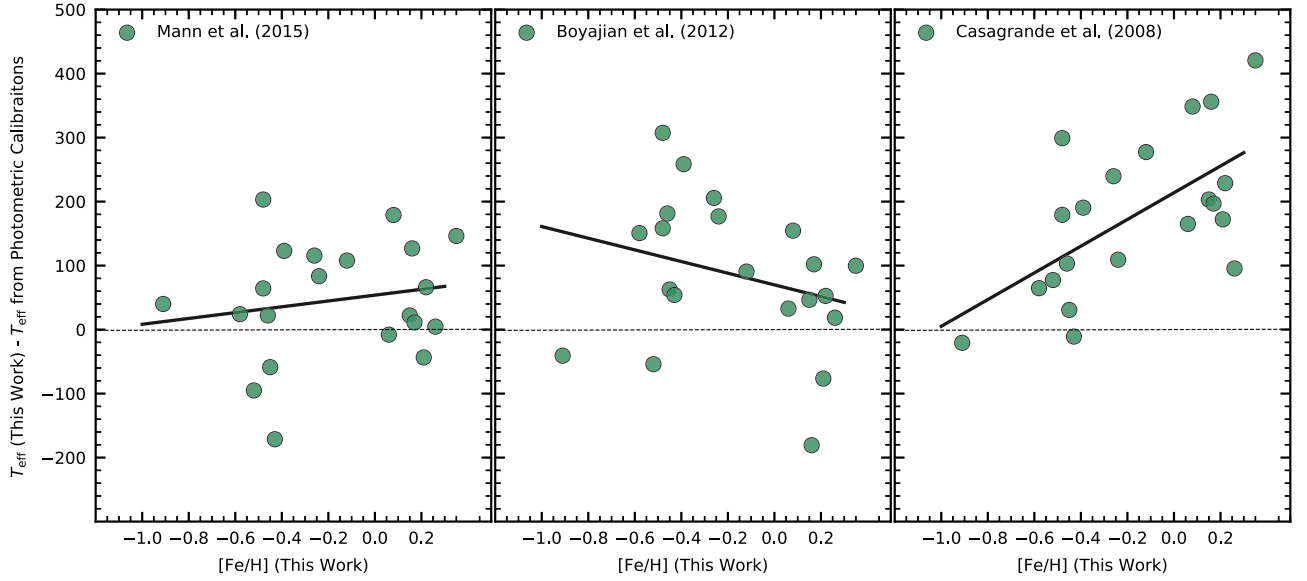
Figure 8. The differences ($\delta T_{\rm eff}$) between the effective temperatures derived here from APOGEE spectra and those also derived in this study but using photometric calibrations from the literature by Mann et al. (2015, left panel), Boyajian et al. (2012, middle panel), and Casagrande et al. (2008, right panel). The photometric results correspond to the average $T_{\rm eff}$ obtained from the colors $V-J$, $r-J$, $V-H$, and $V-K_s$ (when available). The differences are shown vs. the stellar metallicity obtained in this study, indicating systematic trends that are represented by solid lines corresponding to simple linear regressions to $\delta T_{\rm eff}$–[Fe/H].
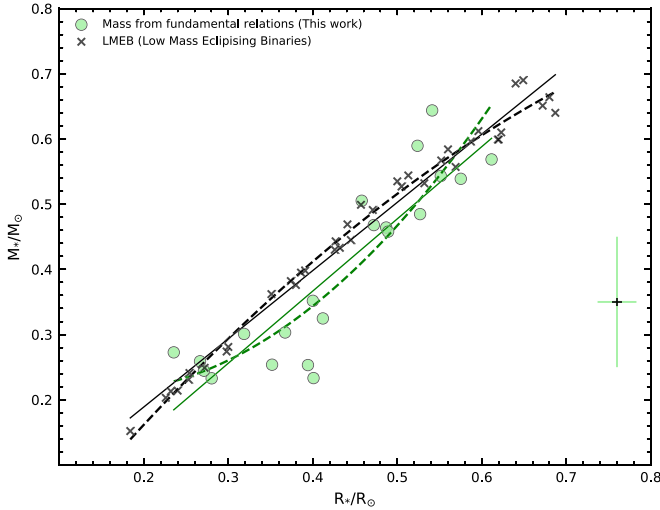
Figure 9. The M dwarf $R_\star/R_\odot$–$M_\star/M_\odot$ diagram for the studied stars. The green circles represent the results of this work, and the black crosses are from eclipsing binaries M dwarfs. Linear and quadratic best fits are show as solid and dashed lines (the line colors represent the respective works). The typical error bar for the $R_\star/R_\odot$ and $M_\star/M_\odot$ is shown in the bottom-right panel of the figure.

Figure 10. The M dwarf M_{K_S}–$R_\star/R_\odot$ diagram for the studied stars. We overplot two best fits to the data, where the solid and dashed lines represent one- and two-degree polynomial fits, respectively.

results from the different studies, noting that these were quite consistent (typical standard deviations of 0.05 dex or less).

In Figure 11, we show the comparison between the metallicity scale for the 11 M dwarfs in binary systems with results obtained from the literature for the warmer primaries (Table 2). Most of the studied stars have metallicities [Fe/H] > -0.8, with the exception of one star that is more metal poor. Overall, the agreement between the results is good with a mean difference of $\langle$[Fe/H](this work) $-$ [Fe/H](primaries)$\rangle = +0.04 \pm 0.18$ dex. The systematic offset of $+0.04$ dex is small (and not statistically significant), in particular when considering the very different effective temperature regimes of the two samples (M dwarfs

versus FGK-type stars), the different methodologies and spectral lines analyzed (although Fe I lines are analyzed both in the optical and NIR, these are from different excitation potentials, multiplets, etc.), as well as the spectral regions analyzed (here APOGEE spectra cover 1.5–1.7 μm, versus optical spectra for the FGK stars).

The typical uncertainties in our derived iron abundances are about $\sim$0.10 dex (see Souto et al. 2017, 2018), while the reported uncertainties in [Fe/H] for the primary stars in the literature are $\sim$0.06 dex (not accounting for possible systematic differences in the metallicities for the different adopted works). Based on these uncertainties, we can conclude that the metallicities from the M dwarfs derived in this study compare well with metallicities from the warmer primary stars within the uncertainties.
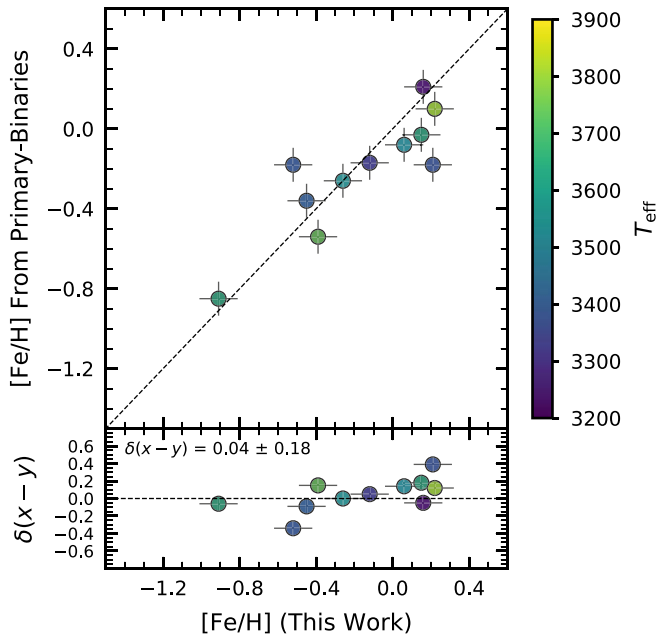
Figure 11. The metallicity scale for the M dwarfs in this study compared with the metallicities compiled from the literature for the primary FGK stars. The diagram is shown at the bottom panel.

Table 2
Primary Stars' Metallicities

2Mass ID	ID (primary)	[Fe/H]	Source
Binaries			
2M03044335+6144097	HIP 14286	-0.26 ± 0.05	e, i, j
2M03150093+0103083	HIP 15126	-0.85 ± 0.05	d, h, k, l
2M03553688+5214291	HIP 18366	-0.36 ± 0.05	d, k
2M06312373+0036445	HIP 31127	-0.54 ± 0.04	h
2M08103429−1348514	HIP 40035	-0.08 ± 0.06	d, g, k
2M12045611+1728119	HIP 58919	-0.18 ± 0.06	b
2M14045583+0157230	HIP 68799	-0.03 ± 0.04	h
2M18244689−0620311	HIP 90246	-0.18 ± 0.04	a, d, h
2M20032651+2952000	HIP 98767	0.21 ± 0.05	c, d, k, l
2M02361535+0652191	HIP 12114	-0.17 ± 0.05	f, i, k
2M05413073+5329239	HIP 26779	0.10 ± 0.05	j, l

Source: (a) Adibekyan et al. (2012); (b) Montes et al. (2018); (c) Bensby et al. (2014); (d) Carretta et al. (2013); (e) De Silva et al. (2015); (f) Ghezzi et al. (2010); (g) Lambert & Reddy (2004); (h) Mann et al. (2013a); (i) Mishenina et al. (2008); (j) Ramírez et al. (2007); (k) Ramírez et al. (2012); (l) Reddy et al. (2006).

6. Conclusions

We have utilized high-resolution near-IR spectra of 21 M dwarfs, observed as part of the SDSS IV APOGEE survey, to explore and develop new, purely spectroscopic analysis techniques that can be used to derive fundamental parameters for these cool stars, including atmospheric parameters ($T_{\rm eff}$ and log g), as well as metallicities (Fe and O). This sample contains 11 secondary M-dwarf stars in binary systems that have hotter FGK main-sequence primaries, plus 10 M dwarfs with interferometric radii measured in the literature. Quantitative spectroscopic analyses, which use combinations of H_2O and OH lines to determine self-consistent values of $T_{\rm eff}$, log g, and O abundances via LTE calculations, have been developed.

We find good agreement, within the uncertainties, in the spectroscopic $T_{\rm eff}$s derived here when compared to results from the literature for stars in common, although the M-dwarf effective temperatures obtained are slightly higher than those derived by photometric relations.

The metallicities of M dwarfs in binary systems derived here, when compared to those from the literature for the warmer primaries, are in excellent agreement, with no trends with the star's $T_{\rm eff}$. These results can be used to help calibrate the APOGEE automated ASPCAP (García Pérez et al. 2016) pipeline to produce improved abundances for the M dwarfs observed in the APOGEE survey.

The independent spectroscopic parameters $T_{\rm eff}$ and log g derived in this study can be used, in conjunction with *Gaia* distances, to calculate the fundamental M-dwarf quantities of radius and mass, which can be compared to radii and masses derived from other techniques. The radii found here via our high-resolution spectroscopic analysis are slightly smaller (by $\sim$0.01 $R_\star/R_\odot$) than the radii inferred from the interferometric observations of Boyajian et al. (2012). Combining the M-dwarf radii determined here with the spectroscopically derived values of log g results in M-dwarf masses that agree reasonably well with those found via analyses of M-dwarf members of eclipsing binary systems, though there is a systematic offset of $\sim$5%–10%, in the sense that our masses are slightly smaller at a given stellar radius.

The results obtained here, based on a pure, high-resolution spectroscopic analysis of the APOGEE *H*-band spectra of M dwarfs, are important and will help to improve the accuracy of the ASPCAP results for tens of thousands of M dwarfs, whose scientific importance has increased over the last years due to the discoveries of many "Earth-like" exoplanets orbiting some M-dwarf stars.

ORCID iDs

Diogo Souto ⍟ https://orcid.org/0000-0002-7883-5425
Katia Cunha ⍟ https://orcid.org/0000-0001-6476-0576
C. Allende Prieto ⍟ https://orcid.org/0000-0002-0084-572X
Adam Burgasser ⍟ https://orcid.org/0000-0002-6523-9536
Kevin Covey ⍟ https://orcid.org/0000-0001-6914-7797
Jon A. Holtzman ⍟ https://orcid.org/0000-0002-9771-9622
Jennifer A. Johnson ⍟ https://orcid.org/0000-0001-7258-1834
Henrik Jönsson ⍟ https://orcid.org/0000-0002-4912-8609
Suvrath Mahadevan ⍟ https://orcid.org/0000-0001-9596-7983
Steven R. Majewski ⍟ https://orcid.org/0000-0003-2025-3147
Matthew Shetrone ⍟ https://orcid.org/0000-0003-0509-2656
Keivan G. Stassun ⍟ https://orcid.org/0000-0002-3481-9052
Ryan Terrien ⍟ https://orcid.org/0000-0002-4788-8858

References

Abolfathi, B., Aguado, D. S., Aguilar, G., et al. 2018, ApJS, 235, 42
Adibekyan, V. Z., Sousa, S. G., Santos, N. C., et al. 2012, A&A, 545, A32
Ahumada, R., Allende Prieto, C., Almeida, A., et al. 2019, arXiv:1912.02905
Alam, S., Albareti, F. D., Allende Prieto, C., et al. 2015, ApJS, 219, 12
Allard, F., Hauschildt, P. H., & Schwenke, D. 2000, ApJ, 540, 1005
Allard, F., Homeier, D., Freytag, B., et al. 2013, MSAIS, 24, 128
Alvarez, R., & Plez, B. 1998, A&A, 330, 1109
Ammons, S. M., Robinson, S. E., Strader, J., et al. 2006, ApJ, 638, 1004
Bailer-Jones, C. A. L., Rybizki, J., Fouesneau, M., Mantelet, G., & Andrae, R. 2018, AJ, 156, 58
Baraffe, I., Homeier, D., Allard, F., & Chabrier, G. 2015, A&A, 577, A42
Barber, R. J., Tennyson, J., Harris, G. J., & Tolchenov, R. N. 2006, MNRAS, 368, 1087
Bass, G., Orosz, J. A., Welsh, W. F., et al. 2012, ApJ, 761, 157
Batalha, N. M., Rowe, J. F., Bryson, S. T., et al. 2013, ApJS, 204, 24
Bean, J. L., Sneden, C., Hauschildt, P. H., Johns-Krull, C. M., & Benedict, G. F. 2006, ApJ, 652, 1604
Bensby, T., Feltzing, S., & Oey, M. S. 2014, A&A, 562, A71
Blackwell, D. E., Shallis, M. J., & Selby, M. J. 1979, MNRAS, 188, 847
Blanton, M. R., Bershady, M. A., Abolfathi, B., et al. 2017, AJ, 154, 28
Bonfils, X., Delfosse, X., Udry, S., et al. 2005, A&A, 442, 635
Boyajian, T. S., von Braun, K., van Belle, G., et al. 2012, ApJ, 757, 112
Bressan, A., Marigo, P., Girardi, L., et al. 2012, MNRAS, 427, 127
Carretta, E., Gratton, R. G., Bragaglia, A., et al. 2013, ApJ, 769, 40
Carter, J. A., Fabrycky, D. C., Ragozzine, D., et al. 2011, Sci, 331, 562
Casagrande, L., Flynn, C., & Bessell, M. 2008, MNRAS, 389, 585
Charbonneau, D., & Deming, D. 2007, arXiv:0706.1047
Covey, K. R., Lada, C. J., Román-Zúñiga, C., et al. 2010, ApJ, 722, 971
De Silva, G. M., Freeman, K. C., Bland-Hawthorn, J., et al. 2015, MNRAS, 449, 2604

Deshpande, R., Blake, C. H., Bender, C. F., et al. 2013, AJ, 146, 156
Doyle, L. R., Carter, J. A., Fabrycky, D. C., et al. 2011, Sci, 333, 1602
Dressing, C. D., & Charbonneau, D. 2015, ApJ, 807, 45
Eisenstein, D. J., Weinberg, D. H., Agol, E., et al. 2011, AJ, 142, 72
Feiden, G. A., & Chaboyer, B. 2014, ApJ, 789, 53
Gaia Collaboration, Brown, A. G. A., Vallenari, A., et al. 2018, A&A, 616, 1
Gaidos, E., Haghighipour, N., Agol, E., et al. 2007, Sci, 318, 210
Gaidos, E., & Mann, A. W. 2014, ApJ, 791, 54
Gaidos, E., Mann, A. W., Lépine, S., et al. 2014, MNRAS, 443, 2561
García Pérez, A. E., Allende Prieto, C., Holtzman, J. A., et al. 2016, AJ, 151, 144
Ghezzi, L., Cunha, K., Smith, V. V., et al. 2010, ApJ, 720, 1290
Gunn, J. E., Siegmund, W. A., Mannery, E. J., et al. 2006, AJ, 131, 2332
Gustafsson, B., Edvardsson, B., Eriksson, K., et al. 2008, A&A, 486, 951
Hargreaves, R. J., Hinkle, K. H., Bauschlicher, C. W., Jr., et al. 2010, AJ, 140, 919
Hełminiak, K. G., Konacki, M., Różyczka, M., et al. 2012, MNRAS, 425, 1245
Henry, T. J., Jao, W.-C., Winters, J. G., et al. 2018, AJ, 155, 265
Holtzman, J. A., Hasselquist, S., Shetrone, M., et al. 2018, AJ, 156, 125
Hunter, J. D. 2007, CSE, 9, 90
Iglesias-Marzoa, R., Arévalo, M. J., López-Morales, M., et al. 2019, A&A, 627, A153
Irwin, J., Charbonneau, D., Berta, Z. K., et al. 2009, ApJ, 701, 1436
Irwin, J. M., Charbonneau, D., Esquerdo, G. A., et al. 2018, AJ, 156, 140
Irwin, J. M., Quinn, S. N., Berta, Z. K., et al. 2011, ApJ, 742, 123
Jackson, R. J., Deliyannis, C. P., & Jeffries, R. D. 2018, MNRAS, 476, 3245
Johnson, J. A., & Apps, K. 2009, ApJ, 699, 933
Kaeufl, H.-U., Ballester, P., Biereichel, P., et al. 2004, Proc. SPIE, 5492, 1218
Kesseli, A. Y., Kirkpatrick, J. D., Fajardo-Acosta, S. B., et al. 2019, AJ, 157, 63
Kraus, A. L., Tucker, R. A., Thompson, M. I., Craine, E. R., & Hillenbrand, L. A. 2011, ApJ, 728, 48
Lambert, D. L., & Reddy, B. E. 2004, MNRAS, 349, 757
Lepine, S., & Gaidos, E. 2013, AAS Meeting Abstracts, 221, 423.01
Lindgren, S., & Heiter, U. 2017, A&A, 604, A97
Lindgren, S., Heiter, U., & Seifahrt, A. 2016, A&A, 586, A100
López-Morales, M., & Ribas, I. 2005, ApJ, 631, 1120
López-Valdivia, R., Mace, G. N., Sokal, K. R., et al. 2019, ApJ, 879, 105
MacDonald, J., & Mullan, D. J. 2013, ApJ, 765, 126
Majewski, S. R., Schiavon, R. P., Frinchaboy, P. M., et al. 2017, AJ, 154, 94
Mamajek, E. E., Prsa, A., Torres, G., et al. 2015, arXiv:1510.07674
Mann, A. W., Brewer, J. M., Gaidos, E., Lépine, S., & Hilton, E. J. 2013a, AJ, 145, 52
Mann, A. W., Feiden, G. A., Gaidos, E., Boyajian, T., & von Braun, K. 2015, ApJ, 804, 64
Mann, A. W., Gaidos, E., & Ansdell, M. 2013b, ApJ, 779, 188
Martinez, C. F., Cunha, K., Ghezzi, L., & Smith, V. V. 2019, ApJ, 875, 29
Masseron, T., Merle, T., & Hawkins, K. 2016, BACCHUS: Brussels Automatic Code for Characterizing High accUracy Spectra, Astrophysics Source Code Library, ascl:1605.004
McDonald, I., Zijlstra, A. A., & Watson, R. A. 2017, MNRAS, 471, 770
Miller, G. E., & Scalo, J. M. 1979, ApJS, 41, 513
Mishenina, T. V., Soubiran, C., Bienaymé, O., et al. 2008, A&A, 489, 923
Montes, D., González-Peinado, R., Tabernero, H. M., et al. 2018, MNRAS, 479, 1332
Morales, J. C., Ribas, I., Jordi, C., et al. 2009a, ApJ, 691, 1400
Morales, J. C., Torres, G., Marschall, L. A., & Brehm, W. 2009b, ApJ, 707, 671
Muirhead, P. S., Becker, J., Feiden, G. A., et al. 2014, ApJS, 213, 5
Mulders, G. D., Pascucci, I., & Apai, D. 2015, ApJ, 798, 112
Mullan, D. J., & MacDonald, J. 2001, ApJ, 559, 353
Neves, V., Bonfils, X., Santos, N. C., et al. 2014, A&A, 568, A121
Newton, E. R., Charbonneau, D., Irwin, J., et al. 2014, AJ, 147, 20
Nidever, D. L., Holtzman, J. A., Allende Prieto, C., et al. 2015, AJ, 150, 173
Önehag, A., Heiter, U., Gustafsson, B., et al. 2012, A&A, 542, A33
Orosz, J. A., Welsh, W. F., Carter, J. A., et al. 2012a, Sci, 337, 1511
Orosz, J. A., Welsh, W. F., Carter, J. A., et al. 2012b, ApJ, 758, 87
Passegger, V. M., Reiners, A., Jeffers, S. V., et al. 2018, A&A, 615, A6
Plez, B. 2012, Turbospectrum: Code for Spectral Synthesis, Astrophysics Source Code Library, ascl:1205.004
Quirrenbach, A., Amado, P. J., Caballero, J. A., et al. 2014, Proc. SPIE, 9147, 91471F
Rajpurohit, A. S., Allard, F., Teixeira, G. D. C., et al. 2018, A&A, 610, A19
Ramírez, I., Allende Prieto, C., & Lambert, D. L. 2007, A&A, 465, 271
Ramírez, I., Fish, J. R., Lambert, D. L., & Allende Prieto, C. 2012, ApJ, 756, 46

Reddy, B. E., Lambert, D. L., & Allende Prieto, C. 2006, MNRAS, 367, 1329
Ribas, I. 2003, A&A, 398, 239
Rojas-Ayala, B., Covey, K. R., Muirhead, P. S., & Lloyd, J. P. 2012, ApJ, 748, 93
Salpeter, E. E. 1955, ApJ, 121, 161
Schlaufman, K. C., & Laughlin, G. 2010, A&A, 519, A105
Schmidt, S. J., Wagoner, E. L., Johnson, J. A., et al. 2016, MNRAS, 460, 2611
Schweitzer, A., Passegger, V. M., Cifuentes, C., et al. 2019, A&A, 625, A68
Shetrone, M., Bizyaev, D., Lawler, J. E., et al. 2015, ApJS, 221, 24
Shields, A. L., Ballard, S., & Johnson, J. A. 2016, PhR, 663, 1
Skrutskie, M. F., Cutri, R. M., Stiening, R., et al. 2006, AJ, 131, 1163
Souto, D., Cunha, K., García-Hernández, D. A., et al. 2017, ApJ, 835, 239
Souto, D., Unterborn, C. T., Smith, V. V., et al. 2018, ApJL, 860, L15
Suárez Mascareño, A., Rebolo, R., & González Hernández, J. I. 2016, A&A, 595, A12

Terrien, R. C., Mahadevan, S., Deshpande, R., & Bender, C. F. 2015, ApJS, 220, 16
Torres, G., Curtis, J. L., Vanderburg, A., Kraus, A. L., & Rizzuto, A. 2018, ApJ, 866, 67
Torres, G., & Ribas, I. 2002, ApJ, 567, 1140
Tsuji, T., Nakajima, T., & Takeda, Y. 2015, PASJ, 67, 26
Valenti, J. A., Piskunov, N., & Johns-Krull, C. M. 1998, ApJ, 498, 851
Van Der Walt, S., Colbert, S. C., & Varoquaux, G. 2011, CSE, 13, 22
van Leeuwen, F. 2007, Hipparcos, The New Reduction of the Raw Data, Vol. 350 (Berlin: Springer)
Veyette, M. J., Muirhead, P. S., Mann, A. W., et al. 2017, ApJ, 851, 26
Veyette, M. J., Muirhead, P. S., Mann, A. W., & Allard, F. 2016, ApJ, 828, 95
Virtanen, P., Gommers, R., Oliphant, T. E., et al. 2019, arXiv:1907.10121
Wilson, J. C., Hearty, F., Skrutskie, M. F., et al. 2010, Proc. SPIE, 7735, 77351C
Zacharias, N., Finch, C. T., Girard, T. M., et al. 2013, AJ, 145, 44